Original Research Paper

A computer-aided chem-photodynamic drugs self-delivery system for synergistically enhanced cancer therapy

Check for updates

Qiu Wang [a,1], Mengchi Sun [a,1], Chang Li [a], Dan Li [a], Zimeng Yang [a], Qikun Jiang [a], Zhonggui He [a], Huaiwei Ding [b], Jin Sun [a,]*

[a] *Wuya College of Innovation, Shenyang Pharmaceutical University, Shenyang 110016, China*
[b] *Key Laboratory of Structure-Based Drug Design and Discovery, Ministry of Education, Shenyang Pharmaceutical University, Shenyang 110016, China*

ARTICLE INFO

ABSTRACT

The therapeutic strategy that gives consideration to the combination of photodynamic therapy and chemotherapy, has emerged as a potential development of effective anti-cancer medicine. Nevertheless, co-delivery of photosensitizers (PSs) and chemotherapeutic drugs in traditional carriers still remains great limitations due to low drug loadings and poor biocompatibility. Herein, we have utilized a computer-aided strategy to achieve a desired carrier-free self-delivery of pyropheophorbide a (PPa, a common PS) and podophyllotoxin (PPT, a classical chemotherapeutic drug) for synergistic cancer therapy. First, the computational simulation method identified the similar molecular sizes and rigid molecular structures between two drugs molecules. Based on the molecular docking, the intermolecular interactions were found to include π-π stackings, hydrophobic interactions and hydrogen bonds. Next, both drugs could co-assemble into nanoparticles (NPs) via one-step nanoprecipitation method. The various spectral experiments (UV, IR and FL) were conducted to evaluate the formation mechanism of spherical NPs. Moreover, *in vitro* and *in vivo* experiments systematically demonstrated that PPT/PPa NPs not only showed better cellular uptake efficiency, stronger cytotoxicity and higher accumulation in tumor sites, but also exhibited synergistic antitumor effect in female BALB/C bearing-4T1 tumor mice. Such a computer-aided design strategy of chem-photodynamic drugs self-delivery systems pave the way for efficient synergistic cancer therapy.

---

* Corresponding Author.
 E-mail addresses: dinghuaiwei627@163.com (H.W. Ding), sunjin@syphu.edu.cn (J. Sun).
[1] These authors contributed equally to this work.
 Peer review under responsibility of Shenyang Pharmaceutical University.

1. Introduction

Cancer is a major threat to human health and life in the world. Chemotherapy is still a predominant therapeutic modality in the clinical treatment of cancer [1]. Photodynamic therapy (PDT), another promising therapeutic strategy, has been widely used in the treatment of various cancers due to its noninvasive, less undesired side effects and high selectivity [1-3]. In the process of PDT, photosensitizers (PSs) are activated by laser irradiation of specific wavelength and then produce reactive oxygen species (ROS) including singlet oxygen ($^1O_2$), hydrogen peroxide (H_2O_2) and superoxide radical (O^{2-}), to elicit tumor cells death or apoptosis [4-6]. Given different antineoplastic mechanisms, PDT together with chemotherapy has used to potentiate the antitumor effects.

Nano-drug delivery systems (nano-DDS) have been employed to co-deliver chemotherapeutic agents and PSs for synergistic cancer therapy [7-9]. However, most of the prepared procedure of nano-DDSs are typically sophisticated and difficult to promise reproducibility and quality control [10]. In addition, traditional carrier-based nano-DDSs are still far from satisfactory due to low drug loading and poor biocompatibility [11]. Therefore, it is highly desired to precisely design novel nano-systems to solve above dilemmas.

To construct the ingenious high-loading co-delivery systems of chemotherapeutic drugs and PSs, more attention has been paid to the computation simulation on the rational design of a stable nano-DDS [12,13]. For example, our team reported that well-designed dipeptide-based supramolecular nanocarrier could efficiently deliver camptothecin based on the structure-based virtual screening technique [14]. In addition, Zhang and his co-workers have also proved the formation mechanism of 1,1′-dioctadecyl- 3,3,3′,3′-tetramethylindotricarbocyanine iodide (DiR) self-assemblies with the assistance of molecular docking [15].

Podophyllotoxin (PPT), a potent anti-tubulin agent, can significantly inhibit P-glycoprotein-mediated multidrug resistant (MDR) of tumor cells [16-18]. Moreover, it has also been reported that PPT could increase intracellular ROS levels, which was ascribed to PPT-induced cells apoptosis via acting on the S phase of the cell cycle [19]. Nevertheless, PPT has poor water solubility, non-selective distribution and low maximum tolerated dose, hindering its clinical application [20,21].

Herein, the similarities in molecular properties between PPT and pyropheophorbide a (PPa, a common PS) were firstly investigated by dynamic simulations. Meanwhile, the intermolecular interactions between them were also evaluated via molecular docking. A novel chem-photodynamic drugs self-delivery system (PPT/PPa NPs) was reasonably built. By the *in vitro* and *in vivo* experiments, PPT/PPa NPs showed better cellular uptake efficiency, stronger cytotoxicity and larger accumulation amount at tumor tissues than that of PPa solution. Notably, PPT/PPa NPs exhibited great synergistic anti-tumor effect in 4T1 breast tumor xenograft model compared with the mixture of PPT and PPa. Such computer-aided self-delivery nanoplatform of combinational chem-PDT has been a promising strategy in future clinical applications.

2. Materials and methods

2.1. Materials

PPa was supplied by Shanghai Dibai Chemical Technology Co. Ltd (China). DSPE-PEG$_{2K}$ was obtained from Shanghai Advanced Vehicle Technology Co. Ltd (China). Podophyllotoxin (PPT), cell culture medium RPMI 1640, penicillin-streptomycin, fetal bovine serum (FBS), cellular ROS detection assay kit (2,7-dichlorodihydrofluorescein diacetate, DCFH-DA) and Hoechst were purchased from Dalian Meilun Biotech Co., Ltd (China). 3-(4,5-dimthyl-2-thiazolyl)-2,5-dipphenyl-2H-terazolium bromide (MTT) and trypsin-EDTA were brought from Sigma-Aldrich (USA). Other regents and chemicals applied in the article were analytical or HPLC grade.

2.2. The molecular interactions between PPT and PPa

The molecular docking was utilized to assess the molecular interactions between PPT and PPa. The 3-dimentional planar structures of PPT and PPa were acquired by using the Sybyl software. Docking of PPT and PPa molecules were carried out by AutoDock 4.0. The optimized parameters were exerted on the basis of our previous research [14]. The ultimate results were evaluated by utilizing the Discovery Studio 2017 Visualizer software.

2.3. Cell culture

Murine breast cancer cells (4T1) were cultured with RPMI 1640 medium containing streptomycin (100 µg/ml), 10% FBS and penicillin (100 units/ml). And the cells were maintained in a humidified environment of 5% CO_2 incubator at 37 °C.

2.4. *In vitro synergistic effect of PPa and PPT in different molar ratio*

The synergistic effect of PPT and PPa *in vitro* was evaluated via MTT analysis. 4T1 cells (2000 cells/well) were incubated in 96-well cell culture plates for 12 h. Thereafter, the culture medium was replaced by sterile PPT solution, PPa solution and PPT/PPa NPs (PPT/PPa, the molar ratio of 1:5-5:1). After incubation for 4 h, 96-well plates were exposed to 660 nm laser at a photodensity of 25 mW/cm² for 3 min. Then, these cells were cultured for another 44 h. Finally, the absorption value of the medium was measured by a microplate reader at 570 nm. The combination index (CI) of PPT and PPa was calculated in line with our previous work [1]. (CI = 1, additivity; CI < 1, synergistic effect; and CI > 1, antagonistic effect)

2.5. *Preparation and characterization of PPT/PPa NPs*

One step nano-precipitation method was used to prepare the PPT/PPa NPs [22]. First, the solution of PPT (2 mg/ml) in methanol, and PPa (2 mg/ml) in methanol and tetrahydrofuran (1:1, v/v) were obtained. Second, the mixed solution of PPa (200 µl) and PPT (78 µl) was dripped into 2 ml deionized distilled water under stirring (800 rpm, 20 min) at 25 °C. Finally, the organic solvent was removed by nitrogen flow on the

solution surface at 37 °C and the volume of solution was adjusted to 2 ml. Moreover, to improve the stability of NPs, pegylated PPT/PPa NPs were fabricated in the same protocol using the mixed solution of PPT, PPa, and DSPE-PEG$_{2K}$ (20 wt%). The hydrodynamic diameter and zeta potential of PPT/PPa NPs were characterized by a Zetasizer (Nano ZS, Malvern Co., UK). The morphology of PPT/PPa NPs was observed by a transmission electron microscopy (TEM) (HITACHI, HT7700, Japan).

2.6. Assembly mechanism of PPT/PPa NPs

The assembly mechanism of PPT/PPa NPs was investigated by ultraviolet (UV), infrared (IR) and fluorescence (FL) spectra, respectively. For UV spectra, PPT, PPa and the mixture of PPT and PPa were dissolved in methanol. PPT/PPa NPs were dispersed in deionized water and 0.2% sodium dodecyl sulfate (SDS), respectively. Then, their UV spectra were characterized by a multi-functional microplate reader (Thermo Scientific, USA). IR spectra of PPT, PPa, the mixture of PPT and PPa, and PPT/PPa NPs (non-PEGylation) were obtained by Flourier transformation infrared spectrometer. FL spectra of free PPa (10 µg/ml) and PPT/PPa NPs (at an equivalent concentration of PPa) were acquired by using a multifunctional microplate reader. In order to further verify the formation mechanism of PPT/PPa NPs, they were incubated with 10 mM urea (forming competitive hydrogen bonds with molecules) and SDS (dissociating the hydrophobic force), respectively [23,24]. The size change of PPT/PPa NPs was measured by DLS.

2.7. Stability of PPT/PPa NPs

The colloidal stability of PPT/PPa NPs was evaluated by monitoring the change of size in PBS (pH 7.4) including 10% FBS for 24 h at 37 °C. And the size change was determined at pre-designed time points (0, 2, 4, 6, 8, 10, 12, 24 h). Moreover, the long-term stability of PPT/PPa NPs stored at 4 °C was also investigated.

2.8. Cellular uptake

The cellular uptake of PPT/PPa NPs was investigated by confocal laser scanning microscopy (CLSM, TCS SP2/AOBS, LEICA, Germany). 4T1 cells were incubated in 24-well plate at a certain density of 5×10^4 cells/well for 12 h. Thereafter, these cells were incubated with free PPa solution (2 µg/ml) or PPT/PPa NPs (2 µg/ml, PPa equivalent) for 1 h, 2 h, 4 h, respectively. After incubation, these cells were rinsed with ice-cold PBS for three times, fixed with 4% paraformaldehyde and stained with Hoechst. Finally, the fluorescence signals of PPa in 4T1 cells were obtained by CLSM.

2.9. Cellular ROS detection in vitro

The production of ROS in 4T1 cells was detected by the active oxygen kit (DCFH-DA). 4T1 cells (at 1×10^5 cells/well) were seeded in 12-well plates for 12 h. Subsequently, the medium containing PPT/PPa NPs (with PPa concentration of 200 ng/ml) or PPT (78 ng/ml) was added to the cells for 4 h. After the medium was displaced with DCFH-DA (10 µg/ml) for 30 min,

the cells were irradiated by a 660 nm laser device (25 mW/cm^2) for 10 min. Finally, the Eclipse Ti-U inverted microscope was used to detect ROS production of PPT/PPa NPs in 4T1 cells.

Moreover, ROS production was analyzed quantitatively by fluorescence method. 4T1 cells (1×10^4 cells/well) were seeded in black 96-well cell-culture plate for 12 h. Then, the cells were treated according to the same procedure described as the qualitative analysis of ROS production. Ultimately, the fluorescence intensities of DCF were determined by microplate reader at excitation of 488 nm and at emission of 525 nm.

2.10. Cell viability evaluation

The cytotoxicity of PPT solution, PPa solution, the mixed solution of PPT and PPa, and PPT/PPa NPs against 4T1 cells were assessed by MTT method. 4T1 cells (2×10^3 cells/well) were cultured in 96-well plates for 12 h at 37 °C. Then the medium was discarded, PPT solution, PPa solution, the mixed solution of PPT and PPa, and PPT/PPa NPs were added to 96-well plates. These cells were incubated for 48 h before standard MTT assay. For photodynamic cytotoxicity, after incubation with the above formulations for 4 h under dark condition, the cells were treated with a laser device (660 nm, 25 mW/cm^2) for 3 min and further cultured for another 44 h. Afterwards, 20 µl MTT (5 mg/ml) was added to these cells for 4 h at 37 °C. After incubation, the medium was displaced with 150 µl DMSO. Finally, the absorption value of the samples at 570 nm was determined by utilizing a microplate reader.

2.11. Animals

All animal experiments were conducted rigorously in accordance with the Guide for Care and Animal Ethics Committee of Shenyang Pharmaceutical University.

2.12. Biodistribution

To investigate the biodistribution of PPT/PPa NPs in vivo, 4T1 bearing-tumor mice model were established. The establishment of tumor model was as follows: female Balb/c mice were first anesthetized with isoflurane, then 4T1 cells (5×10^6 in 100 µl PBS) were subcutaneously injected into the right blank region of the mice's back. When the volume of tumors reached around 300 mm^3, PPa solution (as a control) and PPT/PPa NPs were administrated into mice via tail vein, at an equivalent PPa dose of 5 mg/kg. The mice were killed at 4, 12 and 24 h post-administration. Then major organs (heart, liver, spleen, lung, kidney) and tumors were excised. The imaging system (IVIS) was implemented to determine the biodistribution and fluorescence intensity of PPT/PPa NPs ($n = 3$).

2.13. In vivo synergistic antitumor effect

The synergistic antitumor effect of PPT/PPa NPs was evaluated on 4T1 breast tumor xenograft model. The establishment of subcutaneous 4T1 tumor model of in Balb/c mice was the same as above 2.12. When tumor sizes were about 150 mm^3,
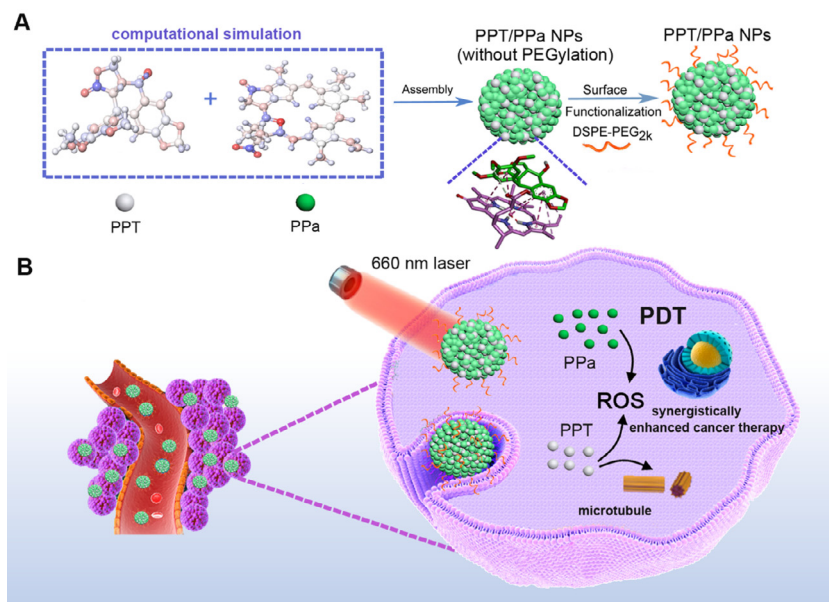
Fig. 1 – Illustration of the preparation process and chem-PDT synergistically enhanced cancer therapy of PPT/PPa NPs with computer-aided design. (A) The computer-aided design of PPT/PPa NPs; The self-delivery nanoassemblies were formed by PPT and PPa based on π-π stackings, hydrophobic interactions and hydrogen bonds existed in two drugs. DSPE-PEG$_{2k}$ was used to functionalize the surface of PPT/PPa NPs to improve the stability. (B) Schematic representation of PPT/PPa NPs for the combination therapy with chemotherapy and PDT under 660 nm laser irradiation.

the 25 mice were randomly divided into 5 groups (n = 5): saline, free PPT solution (2.34 mg/kg), free PPa solution + laser (6 mg/kg), the mixed solution of PPT and PPa + laser, and PPT/PPa NPs + laser (at an equivalent does of PPT and PPa). The mice were injected with the above formulations (200 µl) via tail vein at 0, 2, 4, 6 d. At 12 h post administration, the treated laser groups were irradiated with 660 nm laser for 5 min (200 mW/cm^2). The body weight and tumor volume of the mice were measured every other day (0, 2, 4, 6, 8, 10, 12 d). The volume of the tumor was calculated by the following formula: V=1/2 length × width^2. All mice were sacrificed by cervical vertebra isolation on Day 12. Then the blood samples were obtained to analyze the hepatic and renal function indexes of mice. The tumors and major organs were excised, weighted, and sliced. Finally, the slices were stained with hematoxylin and eosin (H&E) to analyze the physiological changes of mice.

2.14. Statistical analysis

Data were calculated and expressed as mean ± SD. Statistical analysis was implemented with two-tailed student's T-test and one-way analysis of variance (ANOVA) for differences between comparative groups. Significant statistical differences were estimated at $P < 0.05$.

3. Results and discussion

3.1. Investigation on the molecular interactions between PPT and PPa

The dynamic simulations were used to explore the molecular interactions between PPT and PPa. The chemical structures and physicochemical properties of both drugs were showed in Fig. 2A and 2B, respectively. As depicted in Fig. 2C, PPT and PPa had similar molecular sizes, multiple aromatic rings and rigid planar molecular structures, beneficial to form the close intermolecular connections. As shown in Fig. 2D, the results of molecular docking indicated that $\pi-\pi$ stackings, hydrophobic interactions, and intermolecular hydrogen bonds were involved in the interactions between PPT and PPa molecules.

3.2. Preparation and characterization of PPT/PPa NPs

Based on the above results of molecular docking, the preparation of PPT/PPa nanoparticles was attempted through one-step nanoprecipitation method. The PPT/PPa NPs with different molar ratios of PPT to PPa (1:5, 1:2, 1:1, 2:1, 5:1) were established. As shown in Table S1, PPT/PPa NPs had smaller particle size when the molar ratio of PPT to PPa of 1:2 and 1:5. Subsequently, the synergistic effect of the different molar ratios of PPT to PPa was assessed by calculating the CI$_{50}$ (50% inhibition) in 4T1 cells. The CI$_{50}$ of PPT/PPa NPs with molar ratio of PPT to PPa (1:2) was 0.4951, showing the best cytotoxic synergy in 4T1 cells (Table S1). Therefore, the PPT/PPa NPs with molar ratio of 1:2 (PPT/PPa) were elected for further study.

As shown in Fig. 3A, the results of DLS showed that the average diameters of PPT/PPa NPs were approximately 130 nm with a narrow polydispersity index (PDI) of 0.172 ± 0.045. The image of TEM exhibited that PPT/PPa NPs were spherical nanostructures (Fig. 3B) and the zeta potential of PPT/PPa NPs was about -14.8 mV (Fig. S1). The negative surface charge was beneficial for stabilizing the nanoparticles *in vivo*. The
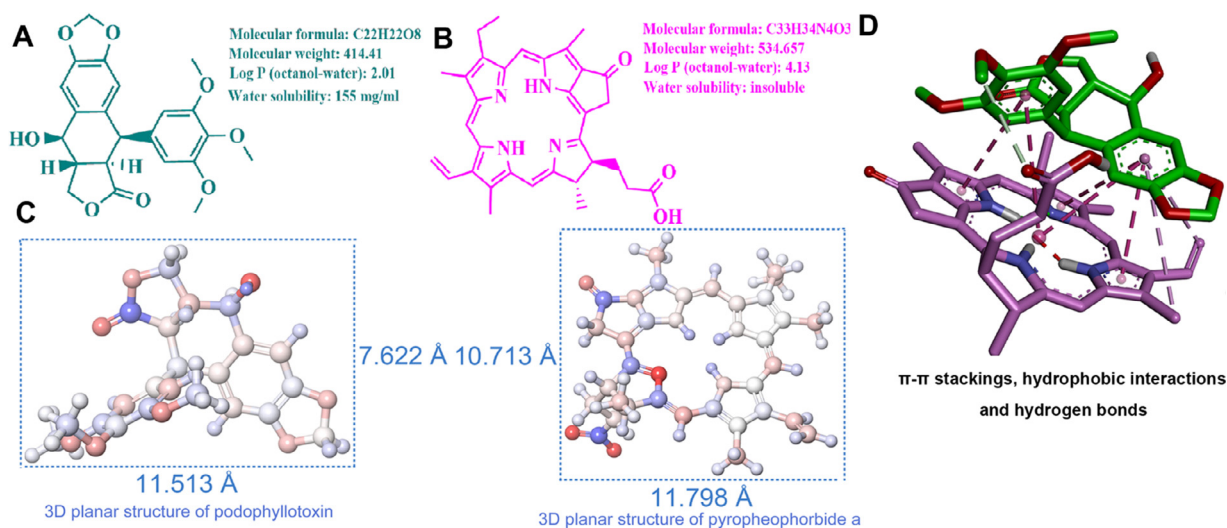
Fig. 2 – The assembly mechanism of PPT/PPa NPs. (A) Chemical structure of podophyllotoxin. (B) Chemical structure of pyropheophorbide a. (C) Three-dimensional grid planar structures and sizes of podophyllotoxin and pyropheophorbide a (Å, angstrom). (D) Computational simulations of the assembly of PPT and PPa in PPT/PPa NPs.
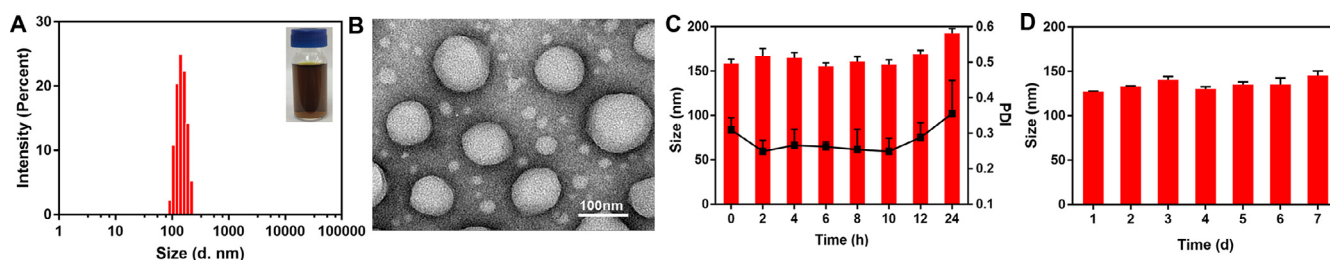
Fig. 3 – Characterization of PPT/PPa NPs *in vitro*. (A) The size distribution profile of PPT/PPa NPs. (B) TEM image of PPT/PPa NPs. (C) Colloidal stability of PPT/PPa NPs in PBS including 10% FBS for 24 h at 37 °C ($n = 3$). (D) Stability of PPT/PPa NPs stored in deionized water at 4 °C for 7 d.
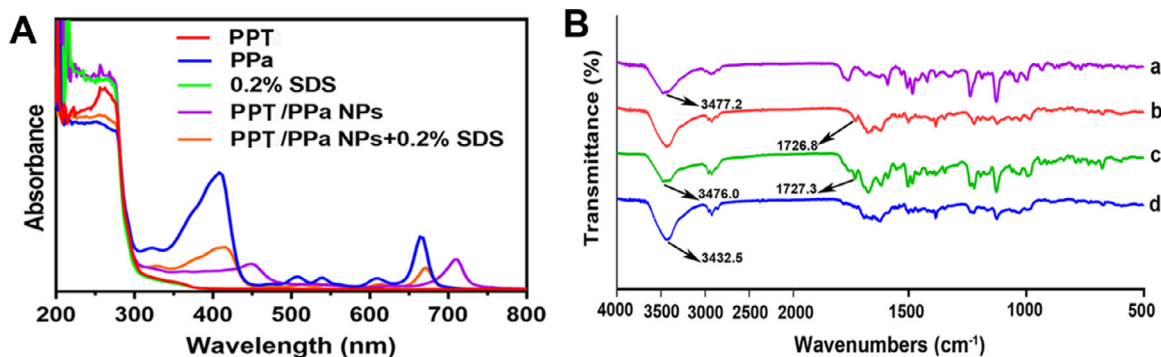
Fig. 4 – Experimental validation of the assembly mechanism of PPT/PPa NPs. (A) UV absorption spectrum of PPT solution, PPa solution, 0.2% SDS, PPT/PPa NPs, and PPT/PPa NPs dissolved in 0.2% SDS. (B) The IR spectrum of PPT (a), PPa (b), the mixture of PPT and PPa (c), and PPT/PPa NPs (d).

colloidal stability of PPT/PPa NPs was further evaluated by incubating NPs in PBS (pH 7.4) containing 10% FBS. The results suggested that the PPT/PPa NPs had a great colloidal stability (Fig. 3C). In addition, the PPT/PPa NPs also exhibited great physical stability in deionized water after being stored at 4 °C for 7 d (Fig. 3D).

3.3.   Formation mechanism of PPT/PPa NPs

The rigorous experiments were conducted to valid the possible formation mechanism of PPT/PPa NPs. As illustrated in Fig. 4A, the UV spectra of PPT/PPa NPs exhibited the evident red shift and widen absorption band compared with PPa
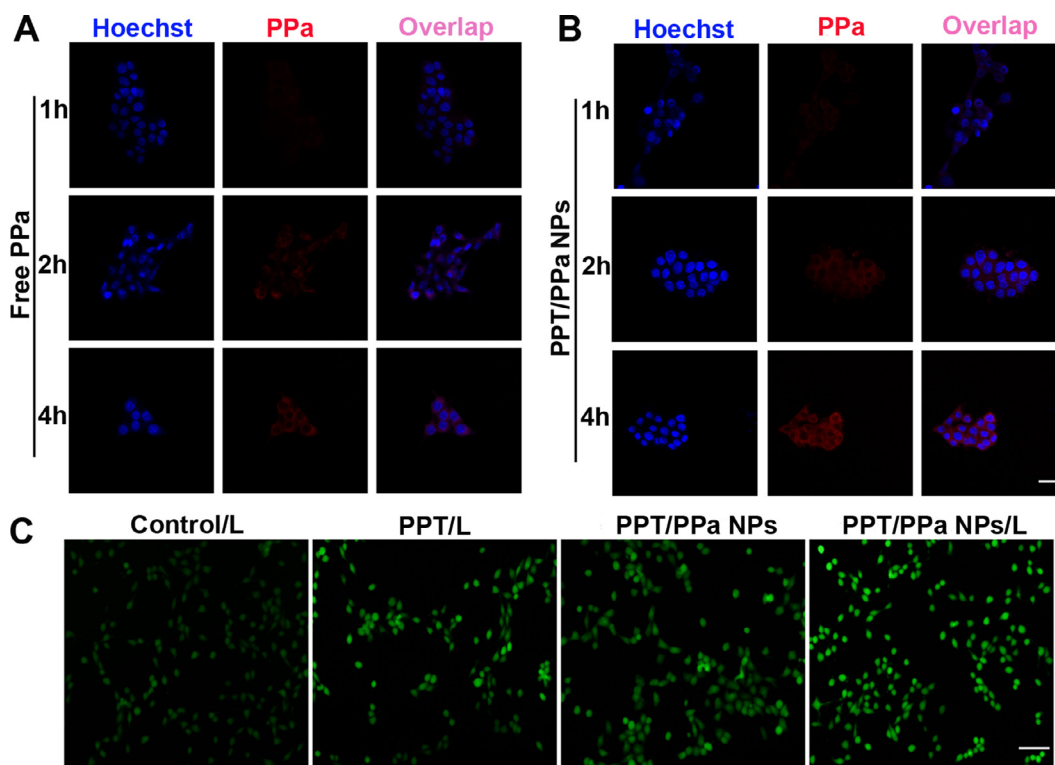
Fig. 5 – Cellular uptake and ROS production of PPT/PPa NPs. (A) The cellular uptake of free PPa in 4T1 cells at 1 h, 2 h and 4 h. (B) The cellular uptake of PPT/PPa NPs in 4T1 cells at 1 h, 2 h and 4 h (the scale bar represents 20 μm). (C) ROS production in 4T1 cells after incubation of PPT/PPa NPs with laser irradiation (25 mW/cm^2, 10 min) or without laser irradiation (the scale bar represents 50 μm).

solution, and the absorption peak of PPT/PPa NPs significantly decreased and almost recovered to the original absorption peak of PPa with the addition of SDS (0.2%, w/v). The results of UV indicated that the strong hydrophobic interactions existed in the PPT/PPa NPs. Besides, the FTIR spectra of PPT/PPa NPs, PPT, PPa and PPT/PPa physical mixture were conducted. As depicted in Fig. 4B, the characteristic peak intensity of carbonyl group υ(C=O) of PPa from PPT/PPa NPs was weaker than that υ(C=O) (1727.0 cm^{-1}) from both PPT/PPa mixture and PPa. Moreover, the hydroxyl (-OH) peaks of PPT became widen and moved to lower wavenumbers, implying that intermolecular hydrogen bond was formed between PPT (-OH) and PPa (C=O). As shown in Fig. S2, the fluorescence intensity of PPa in PPT/PPa NPs decreased compared with free PPa, indicating that PPT/PPa NPs resulted in the fluorescence quenching phenomenon to some extent, due to π–π stacking interactions between PPT and PPa molecules. Moreover, the diameter sizes of urea-/SDS-treated PPT/PPa NPs evidently increased, implying the potential disaggregation of NPs (Fig. S3) [24]. These results were consistent well with that of computational simulations, collectively validating π-π stackings, hydrophobic interactions, and hydrogen bonds served as the drivers to form stable NPs.

3.4. Cellular uptake and ROS detection

CLSM was utilized to compare the cellular uptake efficiency of PPa solution and PPT/PPa NPs. As depicted in Fig. 5A-

5B, The PPa from PPT/PPa NPs exhibited slightly stronger red fluorescence signals than that from PPa solution at 1 h. When the incubation time was prolonged to 2 h and 4 h, the fluorescence signals of PPa from PPT/PPa NPs were significantly enhanced compared to these incubated with free PPa solution. These results showed that PPT/PPa NPs could improve the cellular uptake efficiency compared with PPa solution. Meanwhile, the uptake of PPT/PPa NPs showed a time-dependent manner.

Cellular ROS production was detected by using DCFH-DA staining method. As illustrated in Fig. 5C, PPT could increase ROS production in cells, ascribing to PPT-induced cells apoptosis via acting on the S phase of the cell cycle [12]. The fluorescence intensity of DCF in PPT/PPa NPs was much stronger under laser irradiation compared with no laser irradiation, demonstrating that the PPT/PPa NPs could generate much more ROS with laser irradiation.

In Fig. S4, PPT could elevate the levels of ROS generation in 4T1 cells. In addition, the amount of ROS produced by PPT/PPa NPs with the laser irradiation was much more than that without the laser irradiation. The results were in line with the qualitative analysis of ROS production.

3.5. Cell viability evaluation

The abilities of PPa, PPT, PPT/PPa mixed solution and PPT/PPa NPs to inhibit the growth of 4T1 cells with or without
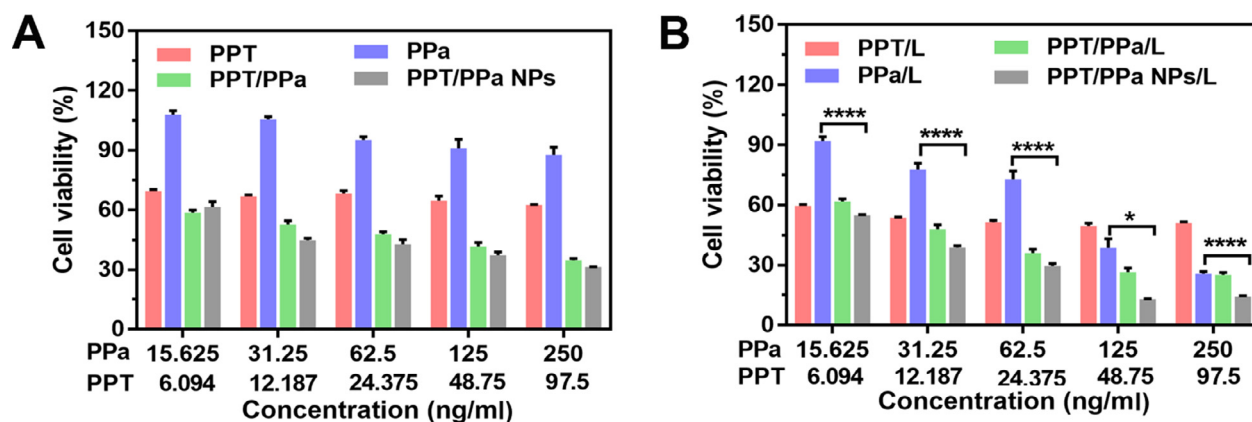
Fig. 6 – The viability of 4T1 cells after incubation of PPT solution, PPa solution, the mixed solution of PPT and PPa (PPT/PPa) and PPT/PPa NPs for 48 h. (A) without laser treatment. (B) with laser treatment (25 mW/cm^2, 3 min); ($n = 3$, *$P < 0.05$, ****$P < 0.0001$).
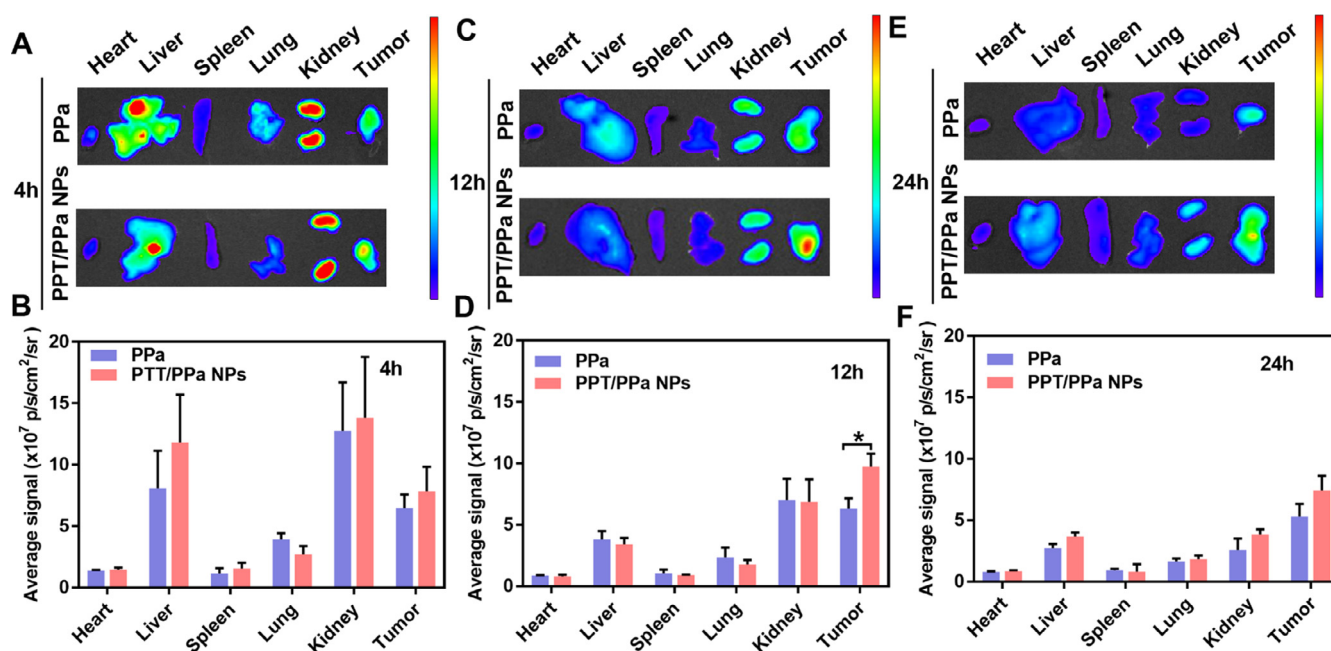
Fig. 7 – The biodistribution of free PPa solution and PPT/PPa NPs in 4T1 xenograft tumor model. *Ex vivo* fluorescence imaging of tumors and major organs at 4 h (A), 12h (C), 24 h (E); Quantitative analysis of fluorescence intensity at 4 h (B), 12 h (D), 24 h (F); (n=3, *$P < 0.05$).

laser irradiation (25 mW/cm^2, 3 min) were investigated by MTT method. As illustrated in Fig. 6, PPT exhibited moderate cytotoxicity against 4T1 cells, which was attributed to inhibition of tubulin and ROS production. PPa showed stronger cytotoxicity under laser irradiation than that without laser irradiation. More importantly, compared to PPT alone and PPa/laser, PPT/PPa NPs laser group exhibited the strongest cytotoxicity against 4T1 cells. Intriguingly, the greatest cytotoxicity of PPT/PPa NPs under laser irradiation was not the simple addition of PPT and PPa, but the synergism

of the two drugs in PPT/PPa NPs (CI of 50% inhibition<1, Table S1).

3.6. Biodistribution of PPT/PPa NPs

The biodistribution of PPT/PPa NPs in major organs and tumors was investigated by 4T1 tumor-bearing mice model. After 4, 12 or 24 h post-administration, imaging and quantitative analysis of free PPa and PPT/PPa NPs in major organs and tumors were determined by an IVIS small animal
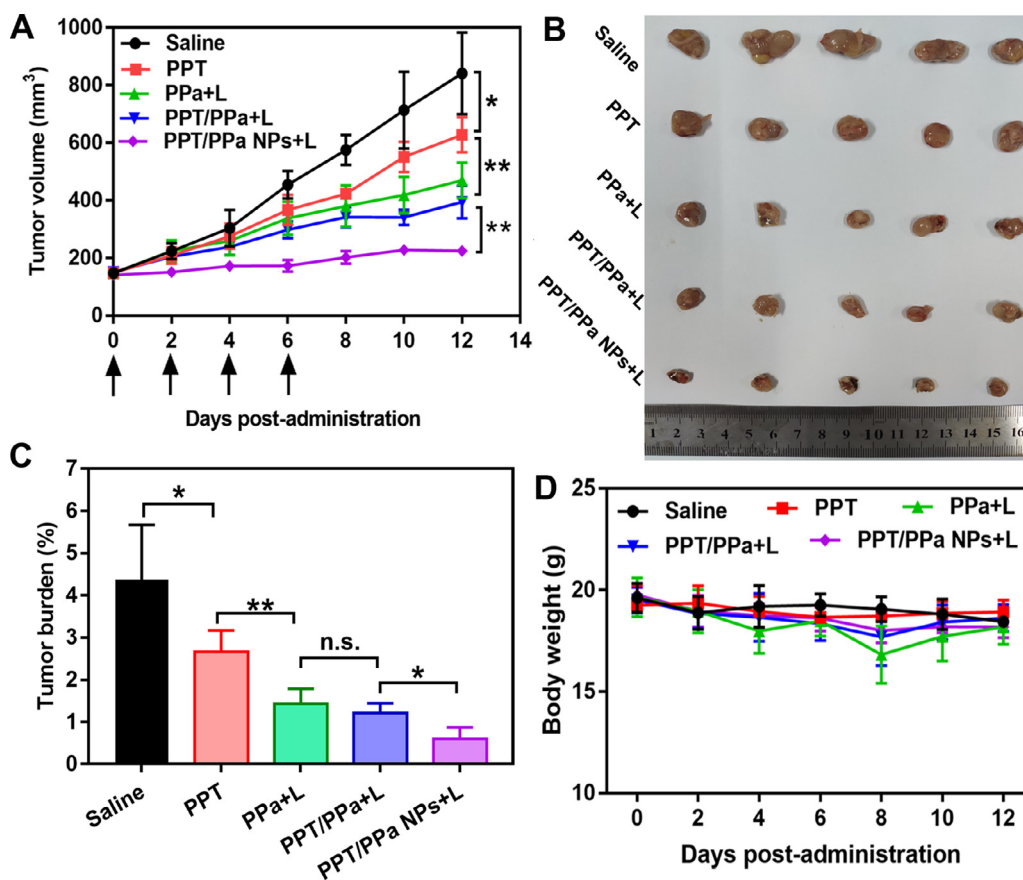
Fig. 8 – *In vivo* synergistic anti-tumor efficacy of PPT/PPa NPs under 660 nm laser treatment (200 mW/cm^2, 5 min). (A) Tumor growth curves treated with different formulations (saline, PPT solution, PPa solution, mixed solution of PPT and PPa, and PPT/PPa NPs). (B) Images of excised tumors on day 12. (C) The tumor burden after the last treatment. (D) Body weight changes of mice in each group. ($n = 5$, n.s. no significance, *P < 0.05, **P < 0.01).

imaging system. As shown in Fig. 7, both free PPa and PPT/PPa NPs exhibited strong fluorescence signals in liver, which were probably attributed to be eliminated by reticuloendothelial systems [25]. The PPa fluorescence intensity of PPT/PPa NPs in tumor sites was always stronger than that of free PPa solution at various time points. The result suggested PPT/PPa NPs had better tumor targeting ability based on the enhanced permeability and retention (EPR) effect of nanomedicines [26]. The accumulation amounts of PPT/PPa NPs in tumor tissues reached the peak at 12 h. So, the optimal time of irradiation was determined at 12 h after administration. Fig. 7A showed that free PPa had high accumulation in kidneys at 4 h, implying that PPa was probably eliminated through the renal route [27].

3.7. *In vivo antitumor efficacy*

In vivo therapeutic efficacy of PPT/PPa NPs was evaluated by 4T1 xenograft tumor model. At 12 h post-administration, PPa solution, PPT/PPa mixture and PPT/PPa NPs were irradiated with 660 nm laser for 5 min (200 mW/cm^2) based on the results of biodistribution. As illustrated in Fig. 8, the tumor

volume of the saline group was approximately 800 mm^3 at day 12. Compared with saline group, the tumor growth of PPT group was moderately inhibited. The group of PPa solution and PPT/PPa mixture showed significant antitumor efficacy compared with the saline group. More importantly, PPT/PPa NPs exhibited the best antitumor efficacy, ascribing to the synergistic tumor ablation of PPT and PPa, and high accumulation of NPs in tumor sites.

Next, we further evaluated the biosafety of the PPT/PPa NPs. As shown in Fig. 8D. the average weight of mice of each group was barely changed during the 12 d. In terms of H&E staining, there was also no significant change in histological morphology of main organs in all groups (Fig. 9A). It was noteworthy that evident necrosis and apoptosis of tumor were observed in the PPT/PPa NPs group (Fig. 9A). Additionally, the serum levels of blood aspartate transaminase (AST), alanine transaminase (ALT), urea nitrogen (BUN) and creatinine (CREA) were used to evaluate liver and renal function. As depicted in Fig. 9B-9E, the levels of AST, ALT, BUN, and CREA were not significantly different among the five groups, indicating that the PPT/PPa NPs had a good biosafety.
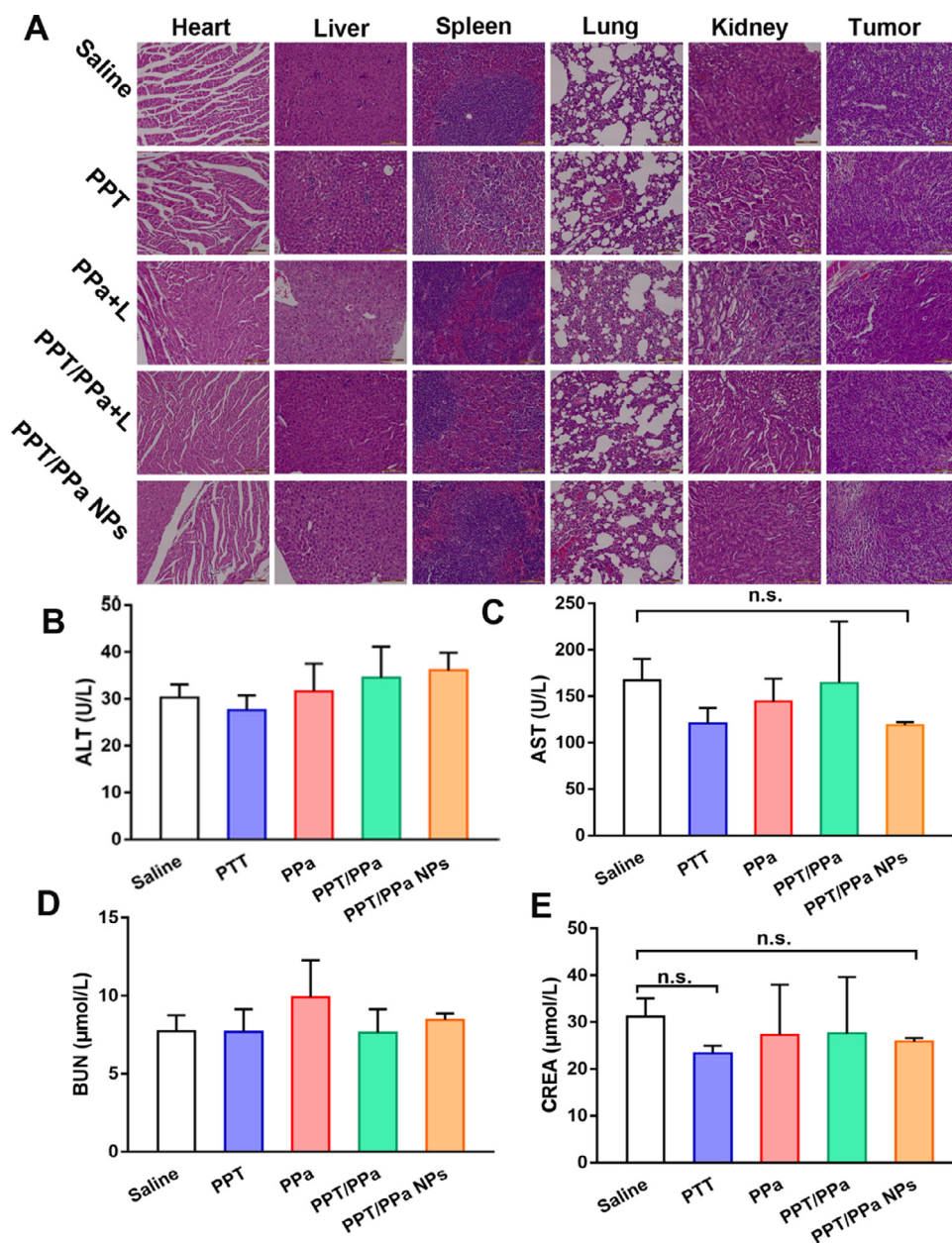
Fig. 9 – The biosafety evaluation *in vivo* of different formulations. (A) The H&E staining results; (B) ALT: alanine aminotransferase; (C) AST: aspartate aminotransferase; (D) BUN: blood urea nitrogen; (E) CREA: creatinine (n=3, n.s. no significance).

4. Conclusions

In this study, a novel self-delivery system (Podophyllotoxin/pyropheophorbide a nanoparticles, PPT/PPa NPs) was reasonably designed and fabricated for synergistic chemo-PDT combination cancer therapy, based on the computational simulations. The similar molecular sizes and rigid planar molecular structures resulted in the potent intermolecular connections between PPT and PPa. Both drugs could successfully co-assemble into NPs through one-step nanoprecipitation method. The PPT/PPa NPs showed excellent colloidal and stored stability in the physiological condition. Furthermore, PPT/PPa NPs also exhibited significant advantages in terms of results *in vitro* and *in vivo*: (i) Compared with free PPa, PPT/PPa NPs showed higher cellular uptake efficiency and remarkably increased cytotoxicity; (ii) PPT/PPa NPs presented high accumulation in tumor tissues; (iii) Most importantly, PPT/PPa NPs-mediated synergetic chemo-PDT contributed to superior antitumor effect. In summary, this rational and efficient strategy with the aid of computational simulations would be of great importance for inspiring more exploration of PDT in combination with chemotherapy in the cancer treatment.

Conflicts of interest

All authors claim no conflict of completing interests.

Acknowledgements

Supplementary materials

Supplementary material associated with this article can be found, in the online version, at doi:10.1016/j.ajps.2020.04.002.

REFERENCES

[1] Luo C, Sun B, Wang C, Zhang X, Chen Q, Yu H, et al. Self-facilitated ROS-responsive nanoassembly of heterotypic dimer for synergistic chemo-photodynamic therapy. J Control Release 2019;302:79–89.

[2] Xu J, Yu S, Wang X, Qian Y, Wu W, Zhang S, et al. High affinity of chlorin e6 to immunoglobulin G for intraoperative fluorescence image-guided cancer photodynamic and checkpoint blockade therapy. ACS nano 2019;13(9):10242–60.

[3] Wang M, Zhai Y, Ye H, Lv Q, Sun B, Luo C, et al. High co-loading capacity and stimuli-responsive release based on cascade reaction of self-destructive polymer for improved chemo-photodynamic therapy. ACS nano 2019;13(6):7010–23.

[4] Sun B, Chen Y, Yu H, Wang C, Zhang X, Zhao H, et al. Photodynamic PEG-coated ROS-sensitive prodrug nanoassemblies for core-shell synergistic chemo-photodynamic therapy. Acta Biomater 2019;92:219–28.

[5] Lin LS, Song J, Song L, Ke K, Liu Y, Zhou Z, et al. Simultaneous fenton-like ion delivery and glutathione depletion by MnO_2-based nanoagent to enhance chemodynamic therapy. Angew Chem Int Ed 2018;57(18):4902–6.

[6] Sun Q, He F, Sun C, Wang X, Li C, Xu J, et al. Honeycomb-satellite structured pH/H_2O_2-responsive degradable nanoplatform for efficient photodynamic therapy and multimodal imaging. ACS Appl Mater Interfaces 2018;10(40):33901–12.

[7] Luo C, Sun J, Sun B, He Z. Prodrug-based nanoparticulate drug delivery strategies for cancer therapy. Trends Pharmacol Sci 2014;35(11):12–22.

[8] Sun B, Luo C, Yu H, Zhang X, Chen Q, Yang W, et al. Disulfide bond-driven oxidation- and reduction-responsive prodrug nanoassemblies for cancer therapy. Nano Lett 2018;18(6):3643–50.

[9] Wei Z, Liang P, Xie J, Song C, Tang C, Wang Y, et al. Carrier-free nano-integrated strategy for synergetic cancer antiangiogenic therapy and phototherapy. Chem Sci 2019;10(9):2778–84.

[10] Chen F, Zhao Y, Pan Y, Xue X, Zhang X, Kumar A, et al. Synergistically enhanced therapeutic effect of a carrier-free HCPT/DOX nanodrug on breast cancer cells through improved cellular drug accumulation. Mol Pharm 2015;12(7):2237–44.

[11] Zhang R, Xing R, Jiao T, Ma K, Chen C, Ma G, et al. Carrier-free, chemophotodynamic dual nanodrugs via self-assembly for synergistic antitumor therapy. ACS Appl Mater Interfaces 2016;8(21):13262–9.

[12] Sun B, Luo C, Zhang X, Guo M, Sun M, Yu H, et al. Probing the impact of sulfur/selenium/carbon linkages on prodrug nanoassemblies for cancer therapy. Nat Commun 2019;10:3211.

[13] Li Y, Liu G, Ma J, Lin J, Lin H, Su G, et al. Chemotherapeutic drug-photothermal agent co-self-assembling nanoparticles for near-infrared fluorescence and photoacoustic dual-modal imaging-guided chemo-photothermal synergistic therapy. J Control Release 2017;258:95–107.

[14] Sun M, Zhang X, Gao Z, Li T, Luo C, Zhao Y, et al. Probing the dipeptide-based supramolecular assembly as an efficient camptothecin delivering carrier for cancer therapy: computational simulations and experimental validations. Nanoscale 2019;11(9):3864–76.

[15] Zhang X, Sun B, Zuo S, Chen Q, Gao Y, Zhao H, et al. Self-assembly of a pure photosensitizer as a versatile theragnostic nanoplatform for imaging-guided antitumor photothermal therapy. ACS Appl Mater Interfaces 2018;10(30):155–62.

[16] Yang C, Xie Q, Zeng X, Tao N, Xu Y, Chen Y, et al. Novel hybrids of podophyllotoxin and formononetin inhibit the growth, migration and invasion of lung cancer cells. Bioorg Chem 2019;85:445–54.

[17] Li Y, Chen M, Yao B, Lu X, Zhang X, He P, et al. Transferrin receptor-targeted redox/pH-sensitive podophyllotoxin prodrug micelles for multidrug-resistant breast cancer therapy. J Mater Chem B 2019;7(38):5814–24.

[18] Roy A, Mark J, Ernsting M, Undzys E, Li SD. A highly tumor-targeted nanoparticle of podophyllotoxin penetrated tumor core and regressed multidrug resistant tumors. Biomaterials 2015;52:335–46.

[19] Ou K, Kang Y, Chen L, Zhang X, Chen X, Zheng Y, et al. H_2O_2-responsive nano-prodrug for podophyllotoxin delivery. Biomater Sci 2019;7(6):2491–8.

[20] Roy A, Zhao Y, Yang Y, Szeitz A, Klassen T, Li SD. Selective targeting and therapy of metastatic and multidrug resistant tumors using a long circulating podophyllotoxin nanoparticle. Biomaterials 2017;137:11–22.

[21] Liu Y, Zhu S, Gu K, Guo Z, Huang X, Wang M, et al. GSH-activated NIR fluorescent prodrug for podophyllotoxin delivery. ACS Appl Mater Interfaces 2017;9(35):29496–504.

[22] Luo C, Sun J, Liu D, Sun B, Miao L, Musetti S, et al. Self-assembled redox dual-responsive prodrug nanosystem formed by single thioether-bridged paclitaxel-fatty acid conjugate for cancer chemotherapy. Nano Lett 2016;16(9):5401–8.

[23] Zhu YX, Jia HR, Pan GY, Ulrich NW, Chen Z, Wu FG. Development of a light-controlled nanoplatform for direct nuclear delivery of molecular and nanoscale materials. J Am Chem Soc 2018;140(11):4062–70.

[24] Feng B, Niu Z, Hou B, Zhou L, Li Y, Yu H. Enhancing triple negative breast cancer immunotherapy by ICG-templated self-assembly of paclitaxel nanoparticles. Adv Funct Mater 2019;30(6):1906605.

[25] Anselmo AC, Gupta V, Zern BJ, Pan D, Zakrewsky M, Muzykantov V, et al. Delivering nanoparticles to lungs while avoiding liver and spleen through adsorption on red blood cells. ACS nano 2013;7(12):11129–37.

[26] Du D, Wang K, Wen Y, Li Y, Li YY. Photodynamic graphene quantum dot: reduction condition regulated photoactivity and size dependent efficacy. ACS Appl Mater Interfaces 2016;8(5):3287–94.

[27] Yang B, Wang K, Zhang D, Sun B, Ji B, Wei L, et al. Light-activatable dual-source ROS-responsive prodrug nanoplatform for synergistic chemo-photodynamic therapy. Biomater Sci 2018;6(11):2965–75.